Catching the bound states in the continuum of a phantom atom in graphene

L. H. Guessi,[1] R. S. Machado,[2] Y. Marques,[2] L. S. Ricco,[2] K. Kristinsson,[3] M. Yoshida,[1] I. A. Shelykh,[3,4,5] M. de Souza,[1,*] and A. C. Seridonio[1,2]

[1]*IGCE, Unesp–Universidade Estadual Paulista, Departamento de Física, 13506-900, Rio Claro, SP, Brazil*

[2]*Departamento de Física e Química, Unesp–Universidade Estadual Paulista, 15385-000, Ilha Solteira, SP, Brazil*

[3]*Division of Physics and Applied Physics, Nanyang Technological University 637371, Singapore*

[4]*Science Institute, University of Iceland, Dunhagi-3, IS-107 Reykjavik, Iceland*

[5]*ITMO University, St. Petersburg 197101, Russia*

(Received 4 March 2015; revised manuscript received 13 May 2015; published 9 July 2015)

We explore theoretically the formation of bound states in the continuum (BICs) in graphene hosting two collinear adatoms situated at different sides of the sheet and at the center of the hexagonal cell, where a phantom atom of a fictitious lattice emulates the six carbons of the cell. We verify that in this configuration the local density of states near the Dirac points exhibits two characteristic features: (i) a cubic dependence on energy instead of a linear one for graphene as found in New J. Phys. **16**, 013045 (2014), and (ii) the formation of BICs as an aftermath of a Fano destructive interference assisted by the Coulomb correlations in the adatoms. For the geometry where adatoms are collinear to carbon atoms, we report an absence of BICs.

DOI: 10.1103/PhysRevB.92.045409 PACS number(s): 72.80.Vp, 07.79.Cz, 72.10.Fk

I. INTRODUCTION

Graphene is a two-dimensional material consisting of an atomic monolayer where carbon atoms build a honeycomb lattice, which is characterized by a band structure exhibiting a massless relativistic dispersion relation in the vicinity of the Dirac cones situated at the corners of the Brillouin zone [1–3]. Recent experimental and theoretical works demonstrated the possibility of effective controllable adsorption of impurities, the so-called adatoms, by an individual graphene sheet [4–6]. These astonishing hallmarks have driven researchers toward a topic of electron tunneling through adatoms in a relativistic environment [7–9]. The variety of adatom geometries considered so far and novel effects predicted are quite broad. For instance, in a system composed of a couple of magnetic adatoms, the exchange coupling results in a highly anisotropic Ruderman-Kittel-Kasuya-Yosida (RKKY) interaction [10,11].

In this context, the scanning tunneling microscope (STM) technique has been recognized as the most efficient experimental tool [12]. Its use allows us to probe the local density of state (LDOS) of the system. Interestingly enough, the latter is governed by the Fano interference effect [13] between direct tunneling from the STM tip to the host and that via the adatom. In addition, the Fano effect forms the basis of the appearance of the so-called bound states in the continuum (BICs).

BICs were first theoretically predicted by von Neumann and Wigner [14] as quantum states with localized square-integrable wave functions appearing above the threshold of a given stationary potential. The solutions of the corresponding Schrödinger equation are characterized by destructive interference between partial waves, which cancel the amplitude of the wave function at large distances from the potential core. Notably, the subject received a revival after the publication of the work of Stillinger and Herrick [15]. Since then, the appearance of BICs was predicted in optical and photonic systems [16–19], setups with peculiar chirality [20], Floquet-Hubbard states induced by a strong oscillating electric field [21], and driven by ac fields [22], among others.

In the domain of carbon-based structures, graphene ribbons were proposed as appropriate candidates for the detection of BICs [23,24]. However, from the perspective of quantum transport, such states are difficult to see. Indeed, as electrons within BICs are not allowed to leak into the continuum, they become invisible in transport experiments. Hence, in order to prove the existence of BICs, novel experimental setups have been proposed that are suitable for their detection, and these setups are of fundamental interest.

In this article, we discuss theoretically the necessary conditions for the appearance of BICs in graphene-adatom systems. We show that such states appear if two collinear adatoms with Coulomb correlations are placed above and below the center of the hexagonal cell, as shown at Fig. 1.

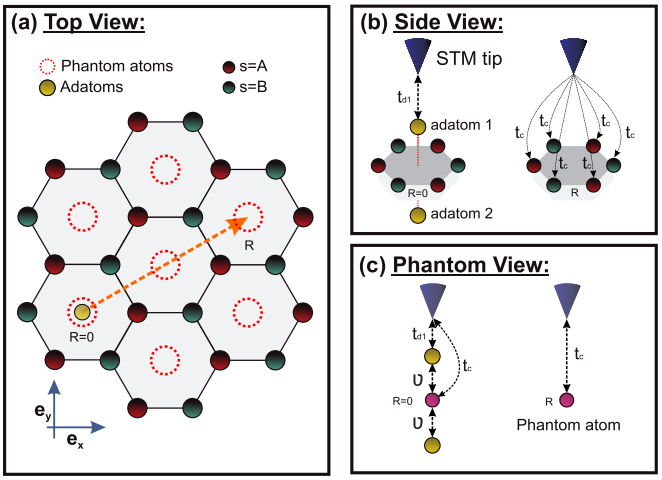

FIG. 1. (Color online) The geometry of the system we consider. (a) The dotted-red circles represent a fictitious lattice composed by phantom atoms in graphene. (b) At the position $\mathbf{R} = \mathbf{0}$, the STM tip couples to the adatom 1 and the six atoms of carbon (only shown for an arbitrary $\mathbf{R}$). (c) Phantom atoms (shaded-red spheres) emulating the cells of (b).

*Present address: Institute of Semiconductor and Solid State Physics, Johannes Kepler University Linz, Austria.

The situation can be considered by means of the introduction of a fictitious or phantom atom located at the center of the hexagonal cell and coupled to the STM tip in the transport experiment. In this configuration, the formation of the BIC is assisted by a Fano interference mechanism. A similar process takes place in the optical and photonic systems described in Refs. [17] and [19]. The phantom atom belongs to a fictitious lattice composed of atoms of the same species, with the density of states (DOS) presenting a cubic energy dependency as was originally predicted by Uchoa *et al.* [8,9]. To make the BIC visible, one needs to introduce the mechanism of its coupling with the continuum, which can be done with use of a detuning between the energy levels of the adatoms.

II. THE MODEL

To provide a theoretical description of the setup presented in Fig. 1, we develop a model based on the two-impurity Anderson Hamiltonian treated in the frameworks of the Hubbard I approximation [25]. The system is described by the model Hamiltonian

$$\mathcal{H}_{\rm T} = \mathcal{H}_{\rm 2D} + \mathcal{H}_{\rm tip} + \mathcal{H}_{\rm tun}. \tag{1}$$

The first term of $\mathcal{H}_{\rm T}$ represents the Anderson-like model,

$$\mathcal{H}_{\rm 2D} = \mathcal{H}_{\rm g} + \mathcal{H}_{\rm d} + \mathcal{H}_{\mathcal{V}}, \tag{2}$$

where the first part corresponds to the free graphene sheet,

$$\mathcal{H}_{\rm g} = -t \sum_{\langle \bar{m},m\rangle\sigma} [\hat{\Psi}^{\dagger}_{A\sigma}(\mathbf{R}_{\bar{m}})\hat{\Psi}_{B\sigma}(\mathbf{R}_m) + \text{H.c.}], \tag{3}$$

in which $\langle \bar{m},m\rangle$ runs over the nearest neighbors of carbon atoms with hopping term $t \approx 2.8$ eV, $\hat{\Psi}^{\dagger}_{s\sigma}(\mathbf{R}_m)$ $[\hat{\Psi}_{s\sigma}(\mathbf{R}_m)]$ is the creation (annihilation) fermionic operator of an electron for a given spin σ in a sublattice $s = A,B$,

$$\mathcal{H}_{\rm d} = \sum_{j\sigma} \mathcal{E}_{jd\sigma} n_{d_j\sigma} + \mathcal{U} \sum_{j} n_{d_j\uparrow} n_{d_j\downarrow} \tag{4}$$

describes the adatoms ($j = 1,2$), where $n_{d_j\sigma} = d^{\dagger}_{j\sigma} d_{j\sigma}$, $d^{\dagger}_{j\sigma}$ ($d_{j\sigma}$) creates (annihilates) an electron with spin σ in the state $\mathcal{E}_{jd\sigma} = \mathcal{E}_d + (-1)^{1-j}\Delta\mathcal{E}$ with the index $j = 1,2$ designating the upper and lower adatoms, respectively, $\Delta\mathcal{E}$ represents the possible detuning between the levels of the different adatoms, $\mathcal{U}$ accounts for the on-site Coulomb interaction, and

$$\mathcal{H}_{\mathcal{V}} = \mathcal{V} \sum_{j=1}^{2} \sum_{i=1}^{3} \sum_{\sigma} \{[\hat{\Psi}_{A\sigma}(\delta_{\mathbf{i}}) + \hat{\Psi}_{B\sigma}(-\delta_{\mathbf{i}})] d^{\dagger}_{j\sigma} + \text{H.c.}\} \tag{5}$$

hybridizes the six atoms of the hexagonal cell with the couple of adatoms as sketched in Fig. 1. $\delta_{\mathbf{1}} = a\mathbf{e}_x$ and $\delta_{2,3} = \frac{a}{2}(-\mathbf{e}_x \pm \sqrt{3}\mathbf{e}_y)$ represent the nearest-neighbor vectors of carbon atoms, $a \sim 1.4$ Å is the distance between graphene atoms, and $\mathcal{V}$ is the hybridization strength, which is supposed to be the same for the six carbons of the hexagonal cell. This assumption holds for adatoms with orbital symmetry: s, f_{z^3}, and d_{z^2} (e.g., Co atoms) [9].

The second part of $\mathcal{H}_{\rm T}$ is described by the Hamiltonian $\mathcal{H}_{\rm tip}$, which corresponds to free electrons in the STM tip. The tunneling Hamiltonian, describing the tip-host coupling, can be expressed as

$$\begin{aligned}\mathcal{H}_{\rm tun} &= \sum_{\sigma} [t_{\rm c}\Psi_{\sigma}(\mathbf{R}) + t_{\rm d1} d_{1\sigma}]\Psi^{\dagger}_{{\rm tip}\sigma} + \text{H.c.} \\ &= t_{\rm c} \sum_{\sigma} \tilde{\Psi}_{\sigma}(\mathbf{R})\Psi^{\dagger}_{{\rm tip}\sigma} + \text{H.c.},\end{aligned} \tag{6}$$

where $\Psi_{{\rm tip}\sigma}$ is the operator for the edge site of the tip, and

$$\Psi_{\sigma}(\mathbf{R}) = \sum_{i=1}^{3} [\hat{\Psi}_{A\sigma}(\mathbf{R} + \delta_{\mathbf{i}}) + \hat{\Psi}_{\mathbf{B}\sigma}(\mathbf{R} - \delta_{\mathbf{i}})] \tag{7}$$

describes the six carbon atoms of the hexagonal cell with its center collinear to the STM tip position $\mathbf{R}$ as outlined at Fig. 1. The field operator

$$\tilde{\Psi}_{\sigma}(\mathbf{R}) = \Psi_{\sigma}(\mathbf{R}) + (t_{\rm d1}/t_{\rm c}) d_{1\sigma} \tag{8}$$

accounts for the quantum interference between the direct electron tunneling through the carbons of such a cell and tunneling through the adatom 1 placed above the central site of the cell. Note that for the ratio $t_{\rm d1}/t_{\rm c} \to 0$, the coupling of the adatom 1 to the STM is negligible compared to the tip-host coupling. The achievement of this regime can be ensured by using an atom with a deeply localized orbital. Such an orbital is characterized by a wave function that is more compact than that of carbon atoms, thus preventing the hopping term $t_{\rm d1}$ from becoming dominant.

After some algebra [26], Eq. (7) can be reduced to

$$\begin{aligned}\Psi_{\sigma}(\mathbf{R} = \mathbf{0}) &= \frac{1}{2\pi}\sqrt{\frac{\pi\Omega_0}{\mathcal{N}}} \sum_{ns} \int \left(\frac{\hbar v_F k}{-t}\right)\sqrt{|k|}\,dk\, c_{nsk\sigma} \\ &\equiv \Psi_{{\rm phantom},\sigma},\end{aligned} \tag{9}$$

which corresponds to the fermionic operator describing the quantum state of the fictitious or phantom atom placed in the center of the hexagonal cell, where n runs over the Dirac points $\mathbf{K}_{\pm} = \mathbf{2\pi/3a}(\mathbf{1}, \pm\mathbf{1}/\sqrt{\mathbf{3}})$.

By applying the linear-response theory, in which the STM tip is considered as a probe, it is possible to show that the differential conductance is determined by

$$G(\mathbf{R}) \sim \frac{e^2}{h}\pi\Gamma_{\rm tip}{\rm LDOS}(\mathbf{R}), \tag{10}$$

where e is the electron charge, $\Gamma_{\rm tip} = 4\pi t_c^2 \rho_{\rm tip}$, $\rho_{\rm tip}$ is the DOS for the tip, and LDOS($\mathbf{R}$) is the LDOS of the phantom atom perturbed by the adatoms, which, despite being a local property, accounts for the entire bath composed by the phantom atoms. It is worth mentioning that if one increases the ratio $t_{\rm d1}/t_{\rm c}$ in Eq. (8), one should treat the coupling to STM on the same footing as the coupling in "graphene+adatoms" system, and as a result, the conductance is not simply proportional to the LDOS, as predicted by the linear-response theory [Eq. (10)]. For the regime of strong coupling between the adatom and the STM tip, the theoretical framework found in Ref. [9] can be applied for the calculation of the conductance. However, as we do not expect the appearance of the BICs in this situation, its detailed analysis is outside the scope of the current work.

To obtain such a LDOS, we first change the system Hamiltonian of Eq. (2) to the momenta domain by performing the transformation

$$\Psi_{s\sigma}(\mathbf{R}_m) = \frac{1}{\sqrt{\mathcal{N}}}\sum_{\mathbf{k}} e^{i\mathbf{k}\cdot\mathbf{R}_m} c_{s\mathbf{k}\sigma}, \tag{11}$$

with $\mathcal{N}$ as the total number of states, $c_{A\mathbf{k}\sigma} = a_{\mathbf{k}\sigma}$, and $c_{B\mathbf{k}\sigma} = b_{\mathbf{k}\sigma}$, which yields the Hamiltonian

$$\begin{aligned}\mathcal{H}_{2D} = &-t\sum_{\mathbf{k}\sigma}[\phi(\mathbf{k})a^{\dagger}_{\mathbf{k}\sigma}b_{\mathbf{k}\sigma} + \text{H.c.}] + \sum_{j\sigma}\mathcal{E}_{jd\sigma}n_{d_{j\sigma}} \\ &+ \mathcal{U}\sum_{j} n_{d_j\uparrow}n_{d_j\downarrow} + \mathcal{V}\sum_{j\sigma}[\Psi_{\sigma}(\mathbf{R}=\mathbf{0})d^{\dagger}_{j\sigma} + \text{H.c.}],\end{aligned} \tag{12}$$

where

$$\Psi_{\sigma}(\mathbf{R}) = \frac{1}{\sqrt{\mathcal{N}}}\sum_{\mathbf{k}} e^{i\mathbf{k}\cdot\mathbf{R}}[\phi(\mathbf{k})a_{\mathbf{k}\sigma} + \phi^{*}(\mathbf{k})b_{\mathbf{k}\sigma}] \tag{13}$$

and $\phi(\mathbf{k}) = \sum_{i=1}^{3} e^{i\mathbf{k}\cdot\delta_i}$.

Next we introduce the retarded Green's function in time domain τ,

$$\mathcal{G}_{\sigma}(\mathbf{R},\tau) = -\frac{i}{\hbar}\theta(\tau)\text{Tr}\{\varrho_{2D}[\tilde{\Psi}_{\sigma}(\mathbf{R},\tau),\tilde{\Psi}^{\dagger}_{\sigma}(\mathbf{R},0)]_{+}\}, \tag{14}$$

where $\theta(\tau)$ is the Heaviside function, ϱ_{2D} is the density matrix of the system described by the Hamiltonian of Eq. (2), and $[\ldots,\ldots]_{+}$ is the anticommutator between operators taken in the Heisenberg picture.

Therefore, the LDOS can be obtained as

$$\text{LDOS}(\mathbf{R}) = -\frac{1}{\pi}\text{Im}\left[\sum_{\sigma}\tilde{\mathcal{G}}_{\sigma}(\mathbf{R},\mathcal{E}^{+})\right], \tag{15}$$

where $\tilde{\mathcal{G}}_{\sigma}(\mathbf{R},\mathcal{E}^{+})$ is the time Fourier transform of $\mathcal{G}_{\sigma}(\mathbf{R},\tau)$. Then by applying the equation of motion (EOM) to the $\mathcal{G}_{\sigma}(\mathbf{R},\tau)$, one can show that near the Dirac points where $t|\phi(\mathbf{k})| = \hbar v_F k$, one has

$$\begin{aligned}\text{LDOS}(\mathbf{R}) &= 2\mathcal{D}_0 + \Delta\text{LDOS}(\mathbf{R}) \\ &= 2\mathcal{D}_0 + \sum_{jl}\Delta\text{LDOS}_{jl}(\mathbf{R}).\end{aligned} \tag{16}$$

Here

$$\mathcal{D}_0 \equiv \mathcal{D}_0^{\text{phantom}} = \frac{1}{\mathcal{N}}\frac{\Omega_0}{\pi(\hbar v_F)^2}\frac{|\mathcal{E}|^3}{t^2} \tag{17}$$

corresponds to the DOS of the fictitious lattice of so-called phantom atoms as depicted in Fig. 1(a). It is worth noticing that such a DOS is spatially independent, as expected for a translational invariant system, thus revealing that the aforementioned lattice is periodic over a set of phantom atoms and encloses the entire energy continuum. This DOS is expressed in terms of the Fermi velocity v_F and the unit cell area Ω_0.

The induced density of states reads

$$\begin{aligned}\Delta\text{LDOS}_{jl}(\mathbf{R}) = &-\Delta\mathcal{D}_0\sum_{\sigma}\text{Im}\{[q_j(\mathbf{R}) - i\mathcal{F}_j(\mathbf{R})]\tilde{\mathcal{G}}_{d_{l\sigma}d_{j\sigma}} \\ &\times [q_l(-\mathbf{R}) - i\mathcal{F}_l(-\mathbf{R})]\}.\end{aligned} \tag{18}$$

It is coordinate-dependent, which is a clear consequence of the breaking of the periodicity of the phantom lattice due to the presence of the adatoms. Clearly, it depends on the Green's functions of the adatoms, namely $\tilde{\mathcal{G}}_{d_{l\sigma}d_{j\sigma}}$ $(j,l = 1,2)$, which can be obtained by determining the time Fourier transform of

$$\mathcal{G}_{d_{l\sigma}d_{j\sigma}}(\tau) = -\frac{i}{\hbar}\theta(\tau)\text{Tr}\{\varrho_{2D}[d_{l\sigma}(\tau),d^{\dagger}_{j\sigma}(0)]_{+}\}. \tag{19}$$

Equation (18) also depends on the position $\mathbf{R}$ of the phantom atom, the Anderson broadening $\Delta = \pi\mathcal{D}_0^{\text{phantom}}\mathcal{V}^2 \propto |\mathcal{E}|^3$, which according to Ref. [9] arises from adatoms with electronic orbitals obeying the C_{3v} group symmetry, such as, for instance, the cases s, f_{z^3}, and d_{z^2}, and

$$q_j(\mathbf{R}) = \frac{1}{\Delta}\text{Re}\Sigma_{\text{phantom}}(\mathbf{R}) + \delta_{j1}(\pi\Delta\mathcal{D}_0)^{-1/2}(t_{\text{d1}}/t_{\text{c}}) \tag{20}$$

is the Fano factor that characterizes the interference between the direct adatom-host and STM-host paths [13] defined by the ratio $t_{\text{d1}}/t_{\text{c}}$. The factor $\mathcal{F}_j(\mathbf{R})$ reads

$$\mathcal{F}_j(\mathbf{R}) = -\frac{1}{\Delta}\text{Im}\Sigma_{\text{phantom}}(\mathbf{R}), \tag{21}$$

where

$$\Sigma_{\text{phantom}}(\mathbf{R}) = \frac{2\mathcal{V}^2}{\mathcal{N}}\sum_{\mathbf{k}}\frac{e^{-i\mathbf{k}.\mathbf{R}}\mathcal{E}^{+}|\phi(\mathbf{k})|^2}{\mathcal{E}^{+2} - t^2|\phi(\mathbf{k})|^2} \tag{22}$$

is the self-energy, which at $\mathbf{R} = \mathbf{0}$ and near the Dirac points can be approximated by

$$\Sigma_{\text{phantom}}(\mathbf{R}=\mathbf{0}) = 2\mathcal{V}^2\frac{\mathcal{E}}{D^2t^2}\left(\mathcal{E}^2\ln\left|\frac{\mathcal{E}^2}{D^2-\mathcal{E}^2}\right| - D^2\right) - i\Delta, \tag{23}$$

as was originally derived in Refs. [8] and [9] ($D \approx 7$ eV denotes the band edge).

From the point of view of the STM-host coupling, a phantom atom emulates a single site beneath the STM tip. Note that the $\mathcal{D}_0$ of Eq. (17) differs from the standard DOS of graphene in the situation of a single carbon connected to a tip, which is characterized by $\mathcal{D}_0^{\text{carbon}} = \Omega_0|\mathcal{E}|/2\mathcal{N}\pi(\hbar v_F)^2$. The cubic dependence $\sim|\mathcal{E}|^3$ at low energies for the phantom DOS arises from the quantum interference between the electron paths through the hexagonal cell: the straight aftermath of such a process is the modification of the band structure of graphene, thus distorting the well-known linear behavior for the DOS when the STM tip position coincides with the center of the hexagon.

To determine the density of states DOS_{jj} of the adatoms at the site $\mathbf{R} = \mathbf{0}$ of the host, we should calculate the Green's functions $\tilde{\mathcal{G}}_{d_{j\sigma}d_{j\sigma}}$:

$$\text{DOS}_{jj} = -\frac{1}{\pi}\text{Im}\left(\sum_{\sigma}\tilde{\mathcal{G}}_{d_{j\sigma}d_{j\sigma}}\right). \tag{24}$$

Toward that end, the Hubbard I approximation can be used [25]. This approach provides reliable results away from the Kondo regime [27]. We start by employing the equation-of-motion (EOM) method to a single-particle retarded Green's function of Eq. (19) in the time domain for an adatom. Going

to the energy domain, one gets

$$(\mathcal{E}^+ - \mathcal{E}_{ld\sigma})\tilde{\mathcal{G}}_{d_{l\sigma}d_{j\sigma}} = \delta_{lj} + \Sigma_{\text{phantom}}(\mathbf{R}=\mathbf{0})\sum_{\bar{l}}\tilde{\mathcal{G}}_{d_{\bar{l}\sigma}d_{j\sigma}} + \mathcal{U}\tilde{\mathcal{G}}_{d_{l\sigma}n_{d_l\bar{\sigma}},d_{j\sigma}}, \quad (25)$$

with $\mathcal{E}^+ = \mathcal{E} + i0^+$. In the equation above, $\tilde{\mathcal{G}}_{d_{l\sigma}n_{d_l\bar{\sigma}},d_{j\sigma}}$ denotes a two-particle Green's function composed of four fermionic operators, obtained by the Fourier transform of

$$\mathcal{G}_{d_{l\sigma}n_{d_l\bar{\sigma}},d_{j\sigma}} = -\frac{i}{\hbar}\theta(\tau)\text{Tr}\{\varrho_{2D}[d_{l\sigma}(\tau)n_{d_l\bar{\sigma}}(\tau),d^\dagger_{j\sigma}(0)]_+\}, \quad (26)$$

where $\bar{\sigma} = -\sigma$ and $n_{d_l\bar{\sigma}} = d^\dagger_{l\bar{\sigma}}d_{l\bar{\sigma}}$. To close the system of the dynamic equations, we obtain the EOM for the Green's function $\mathcal{G}_{d_{l\sigma}n_{d_l\bar{\sigma}},d_{j\sigma}}$, which reads

$$\begin{aligned}(\mathcal{E}^+ - \mathcal{E}_{ld\sigma} - \mathcal{U})\tilde{\mathcal{G}}_{d_{l\sigma}n_{d_l\bar{\sigma}},d_{j\sigma}} &= \delta_{lj}\langle n_{d_l\bar{\sigma}}\rangle + \sum_{\mathbf{ks}}\frac{\mathcal{V}}{\sqrt{\mathcal{N}}}[-\phi_s(\mathbf{k})\tilde{\mathcal{G}}_{c^\dagger_{s\mathbf{k}\bar{\sigma}}d_{l\bar{\sigma}}d_{l\sigma},d_{j\sigma}} \\ &+ \phi^*_s(\mathbf{k})(\tilde{\mathcal{G}}_{c_{s\mathbf{k}\sigma}d^\dagger_{l\bar{\sigma}}d_{l\bar{\sigma}},d_{j\sigma}} + \tilde{\mathcal{G}}_{d^\dagger_{l\bar{\sigma}}c_{s\mathbf{k}\bar{\sigma}}d_{l\sigma},d_{j\sigma}})], \end{aligned} \quad (27)$$

where the index $s = A, B$ marks a sublattice, $c_{A\mathbf{k}\sigma} = a_{\mathbf{k}\sigma}$ and $c_{B\mathbf{k}\sigma} = b_{\mathbf{k}\sigma}$, $\phi_A(\mathbf{k}) = \phi^*(\mathbf{k})$ and $\phi_B(\mathbf{k}) = \phi(\mathbf{k})$, expressed in terms of Green's functions of the same order of $\tilde{\mathcal{G}}_{d_{l\sigma}n_{d_l\bar{\sigma}},d_{j\sigma}}$, and the occupation number can be determined as

$$\langle n_{d_l\bar{\sigma}}\rangle = -\frac{1}{\pi}\int_{-D}^{+D} n_F(\mathcal{E})\text{Im}(\tilde{\mathcal{G}}_{d_{l\bar{\sigma}}d_{l\bar{\sigma}}})d\mathcal{E}, \quad (28)$$

with $n_F(\mathcal{E})$ as the Fermi-Dirac distribution.

Our approach holds for temperatures $T \gg T_K$ (above the Kondo temperature). However, the temperature should not be very high so that we can safely employ the Heaviside step function for the Fermi-Dirac distribution $n_F(\mathcal{E})$ [7]. By employing the Hubbard I approximation, we decouple the Green's functions on the right-hand side of Eq. (27) as follows: $\tilde{\mathcal{G}}_{c^\dagger_{s\mathbf{k}\bar{\sigma}}d_{l\bar{\sigma}}d_{l\sigma},d_{j\sigma}} \simeq \langle c^\dagger_{s\mathbf{k}\bar{\sigma}}d_{l\bar{\sigma}}\rangle\tilde{\mathcal{G}}_{d_{l\sigma}d_{j\sigma}}$ and $\tilde{\mathcal{G}}_{d^\dagger_{l\bar{\sigma}}c_{s\mathbf{k}\bar{\sigma}}d_{l\sigma},d_{j\sigma}} \simeq \langle c^\dagger_{s\mathbf{k}\bar{\sigma}}d_{l\bar{\sigma}}\rangle\tilde{\mathcal{G}}_{d_{l\sigma}d_{j\sigma}}$, where we have used $\sum_{\mathbf{ks}}\phi(\mathbf{k}) = \sum_{\mathbf{ks}}\phi^*(\mathbf{k})$. As a result, we find

$$\begin{aligned}(\mathcal{E}^+ - \mathcal{E}_{ld\sigma} - \mathcal{U})\tilde{\mathcal{G}}_{d_{l\sigma}n_{d_l\bar{\sigma}},d_{j\sigma}} &= \delta_{lj}\langle n_{d_l\bar{\sigma}}\rangle + \frac{\mathcal{V}_j}{\sqrt{\mathcal{N}}}\sum_{\mathbf{ks}}\phi^*_s(\mathbf{k})\tilde{\mathcal{G}}_{c_{s\mathbf{k}\sigma}d^\dagger_{l\bar{\sigma}}d_{l\bar{\sigma}},d_{j\sigma}}. \end{aligned} \quad (29)$$

To complete the calculation, we need to determine $\tilde{\mathcal{G}}_{c_{s\mathbf{k}\sigma}d^\dagger_{l\bar{\sigma}}d_{l\bar{\sigma}},d_{j\sigma}}$. Once again, employing the EOM approach for $\tilde{\mathcal{G}}_{c_{s\mathbf{k}\sigma}d^\dagger_{l\bar{\sigma}}d_{l\bar{\sigma}},d_{j\sigma}}$, we obtain

$$\begin{aligned}\mathcal{E}^+\tilde{\mathcal{G}}_{c_{s\mathbf{k}\sigma}d^\dagger_{l\bar{\sigma}}d_{l\bar{\sigma}},d_{j\sigma}} &= -t\phi_{\bar{s}}(\mathbf{k})\tilde{\mathcal{G}}_{c_{\bar{s}\mathbf{k}\sigma}d^\dagger_{l\bar{\sigma}}d_{l\bar{\sigma}},d_{j\sigma}} \\ &+ \sum_{\mathbf{q}\tilde{s}}\frac{\mathcal{V}_l}{\sqrt{\mathcal{N}}}\phi^*_{\tilde{s}}(\mathbf{q})\tilde{\mathcal{G}}_{c_{s\mathbf{k}\sigma}d^\dagger_{l\bar{\sigma}}c_{\tilde{s}\mathbf{q}\bar{\sigma}},d_{j\sigma}} \\ &+ \sum_{\tilde{j}}\frac{\mathcal{V}_{\tilde{j}}}{\sqrt{\mathcal{N}}}\phi_s(\mathbf{k})\tilde{\mathcal{G}}_{d_{\tilde{j}\sigma}n_{d_l\bar{\sigma}},d_{j\sigma}} \\ &- \sum_{\mathbf{q}\tilde{s}}\frac{\mathcal{V}_l}{\sqrt{\mathcal{N}}}\phi_{\bar{s}}(\mathbf{q})\tilde{\mathcal{G}}_{c^\dagger_{\tilde{s}\mathbf{q}\bar{\sigma}}d_{l\bar{\sigma}}c_{s\mathbf{k}\sigma},d_{j\sigma}}, \end{aligned} \quad (30)$$

where $\bar{s} = A$ and B, respectively, for $s = B, A$ as labels to correlate simultaneously distinct sublattices, while $\tilde{s} = A, B$ runs arbitrarily.

In a similar way, by using the Hubbard I scheme for Eq. (30), we have $\tilde{\mathcal{G}}_{c_{s\mathbf{k}\sigma}d^\dagger_{l\bar{\sigma}}c_{\bar{s}\mathbf{q}\bar{\sigma}},d_{j\sigma}} \simeq \langle d^\dagger_{l\bar{\sigma}}c_{\bar{s}\mathbf{q}\bar{\sigma}}\rangle\tilde{\mathcal{G}}_{c_{s\mathbf{k}\sigma}d_{j\sigma}}$, $\tilde{\mathcal{G}}_{c^\dagger_{\tilde{s}\mathbf{q}\bar{\sigma}}d_{l\bar{\sigma}}c_{s\mathbf{k}\sigma},d_{j\sigma}} \simeq \langle d^\dagger_{l\bar{\sigma}}c_{\tilde{s}\mathbf{q}\bar{\sigma}}\rangle\tilde{\mathcal{G}}_{c_{s\mathbf{k}\sigma}d_{j\sigma}}$, and $\tilde{\mathcal{G}}_{d_{\tilde{j}\sigma}n_{d_l\bar{\sigma}},d_{j\sigma}} \simeq \langle n_{d_l\bar{\sigma}}\rangle\tilde{\mathcal{G}}_{d_{\tilde{j}\sigma}d_{j\sigma}}$, which, in combination with Eqs. (25) and (29), results in

$$\tilde{\mathcal{G}}_{d_{j\sigma}d_{j\sigma}} = \frac{\lambda^{\bar{\sigma}}_j}{\mathcal{E} - \mathcal{E}_{jd\sigma} - \tilde{\Sigma}^\sigma_{jj}}, \quad (31)$$

where $\lambda^{\bar{\sigma}}_j = (1 + \frac{\mathcal{U}\langle n_{d_j\bar{\sigma}}\rangle}{\mathcal{E}-\mathcal{E}_{jd\sigma}-\mathcal{U}-\Sigma_{\text{phantom}}(\mathbf{R}=\mathbf{0})})$, and

$$\tilde{\Sigma}^\sigma_{jj} = \Sigma(\mathbf{R}=\mathbf{0}) + \lambda^{\bar{\sigma}}_j\lambda^{\bar{\sigma}}_{\bar{j}}\frac{[\Sigma_{\text{phantom}}(\mathbf{R}=\mathbf{0})]^2}{\mathcal{E} - \mathcal{E}_{\bar{j}d\sigma} - [\Sigma_{\text{phantom}}(\mathbf{R}=\mathbf{0})]} \quad (32)$$

is the total self-energy, with $\bar{j} = 2, 1$, respectively, for $j = 1, 2$ for the indexes corresponding to distinct adatoms, and

$$\tilde{\mathcal{G}}_{d_{j\sigma}d_{\bar{j}\sigma}} = \frac{\lambda^{\bar{\sigma}}_j\Sigma_{\text{phantom}}(\mathbf{R}=\mathbf{0})\tilde{\mathcal{G}}_{d_{\bar{j}\sigma}d_{\bar{j}\sigma}}}{\mathcal{E} - \mathcal{E}_{jd\sigma} - \Sigma_{\text{phantom}}(\mathbf{R}=\mathbf{0})} \quad (33)$$

are mixed Green's functions, which describe the correlations between the adatoms and are responsible for the Fano destructive interference.

III. RESULTS AND DISCUSSION

In the following discussion, we adopt the following set of system parameters: $t_{d1}/t_c = 10^{-6}$, which ensures the assumption of the STM tip acting as a probe of the "graphene + adatoms" system LDOS as discussed in Sec. II, $\mathcal{E}_d = -0.07D, \mathcal{U} = 0.14D, \mathcal{V} = 0.14D$, and $v_F \approx c/300$ [7].

Figure 2(a) shows a comparison between the linear LDOS of graphene (green curve) versus $\mathcal{D}_0^{\text{phantom}}$ with a cubic dependence characteristic of the phantom atom of Eq. (17) (blue curve). Figure 2(b) displays the densities of states of the adatoms $\text{DOS}_{jj} = \text{DOS}_{11} = \text{DOS}_{22}$ defined by Eq. (24) with zero detuning ($\triangle\mathcal{E} = 0$), where two peaks labeled (1) and (2) are situated within the valence band ($\mathcal{E} < \mathcal{E}_F \equiv 0$) for the case of $\mathcal{U} \neq 0$ (red curve). Two extra peaks appear within the conduction band ($\mathcal{E} > \mathcal{E}_F \equiv 0$) as well (not shown), since we assumed the symmetric Anderson model with the constraint $2\mathcal{E}_d + \mathcal{U} = 0$ being fulfilled. In this regime, the graphene Hamiltonian with adatoms is invariant under particle-hole transformation, and all the properties of the peaks within the conduction band are the same as those within the valence band, thus we do not need to perform a separate analysis for them. Note that deviations from the condition $2\mathcal{E}_d + \mathcal{U} = 0$ will not change the presented results qualitatively, but the positions of the peaks in the conduction and valence bands will no longer be symmetric. For comparison, we also present the curve for $\mathcal{U} = 0$ (dark-dotted curve), characterized by a single peak labeled (3).

Figure 2(c) shows the contributions of the adatoms to the LDOS of graphene. For $\mathcal{U} \neq 0$, the diagonal term $\Delta\text{LDOS}_{jj} = \Delta\text{LDOS}_{11} = \Delta\text{LDOS}_{22}$ displays pronounced peaks at the same energies as the DOS of the adatoms shown at the panel (b). In contrast, the mixing term

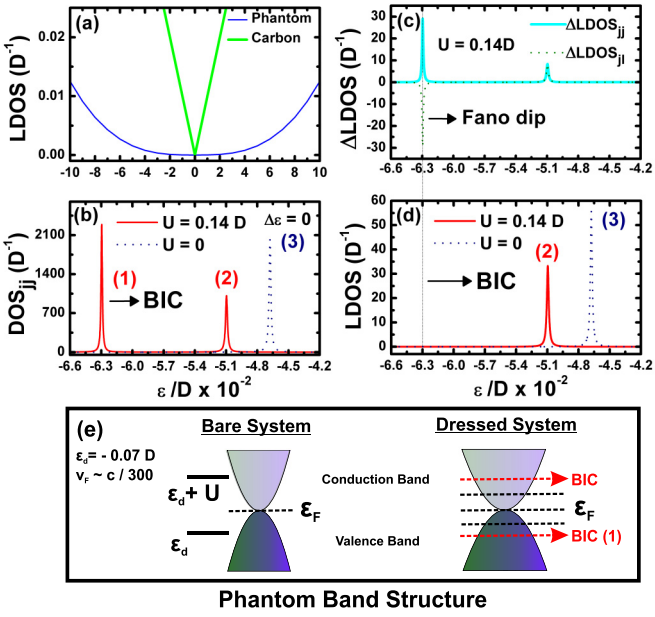

FIG. 2. (Color online) (a) LDOS of graphene coupled to the STM tip for two configurations: the tip above the carbon atom of graphene (labeled as carbon) and the tip in the center of the hexagonal lattice (labeled as phantom). (b) Density of states for the pair of adatoms $\mathrm{DOS}_{jj} = \mathrm{DOS}_{11} = \mathrm{DOS}_{22}$ within the valence band. The parameters are $\mathcal{E}_d = -0.07D, \mathcal{U} = 0.14D, \mathcal{V} = 0.14D$, $v_F \approx c/300$, and $\triangle\mathcal{E} = 0$. Two additional peaks in the conduction band are symmetrically placed if the condition $2\mathcal{E}_d + \mathcal{U} = 0$ is satisfied; those peaks are not shown. (c) Contributions to the LDOS of graphene from the adatom pair. The diagonal contribution shows two pronounced peaks, while the mixing term shows a single pronounced antiresonance. (d) Total LDOS revealing the BIC (marked by vertical line) at the position where the resonance of the diagonal term in the LDOS is compensated by the antiresonance in the mixing term. (e) Sketch of the energy diagram of the system. Left: energy levels without the dressing of the adatoms by conducting electrons. Right: the energy diagram accounting for the Coulomb dressing. The pair of BICs is indicated by red arrows. In both the right and left panels, the coupling of the graphene sheet to the STM tip turns the linear $|\mathcal{E}|$ dependence within the density of states of the host into a cubic one ($|\mathcal{E}|^3$).

$\Delta\mathrm{LDOS}_{jl} = \Delta\mathrm{LDOS}_{12} = \Delta\mathrm{LDOS}_{21}$ exhibits a sharp Fano dip corresponding to the peak located around $\mathcal{E} \approx -6.3 \times 10^{-2}D$. When all contributions to the LDOS are added, this antiresonance cancels exactly the corresponding resonance in the diagonal term. This means that peak (1) of panel (b) can be considered as a BIC arising from a Fano destructive interference assisted by Coulomb correlations: in the situation of a finite Coulomb potential $\mathcal{U}$, $\Delta\mathrm{LDOS}_{jl}$ for $j \neq l$ describes electronic waves that travel forth and back between the upper and lower adatoms, which, for a given energy $\mathcal{E}$, become phase-shifted by π with respect to the waves scattered by the adatoms enclosed by $\Delta\mathrm{LDOS}_{jj}$. In particular, at the sites of the adatoms where the BICs lie and with $\mathcal{E} \approx -6.3 \times 10^{-2}D$, such a condition is fulfilled and is reflected by the peak and Fano dip, respectively, in $\Delta\mathrm{LDOS}_{11} = \Delta\mathrm{LDOS}_{22}$ and $\Delta\mathrm{LDOS}_{12} = \Delta\mathrm{LDOS}_{21}$, as found in Fig. 2(c).

We highlight the fact that the peak in the DOS marked peak (1) in Fig. 2(b) appearing around $\mathcal{E} \approx -6.3 \times 10^{-2}D$ in the red curve does not rise at the same position in the LDOS of panel (d) due to the Fano suppression mechanism, thus preventing the revealing of the BIC by a conductance measurement. This feature is made explicit by the vertical line crossing both panels (c) and (d) in Fig. 2, where the BIC position is marked. We checked that for $\mathcal{U} = 0$, BICs do not appear. For reference purposes, we showed the corresponding peak labeled (3) in Figs. 2(b) and 2(d). In Fig. 2(e), the band structure of the phantom atoms in the presence of BICs is depicted.

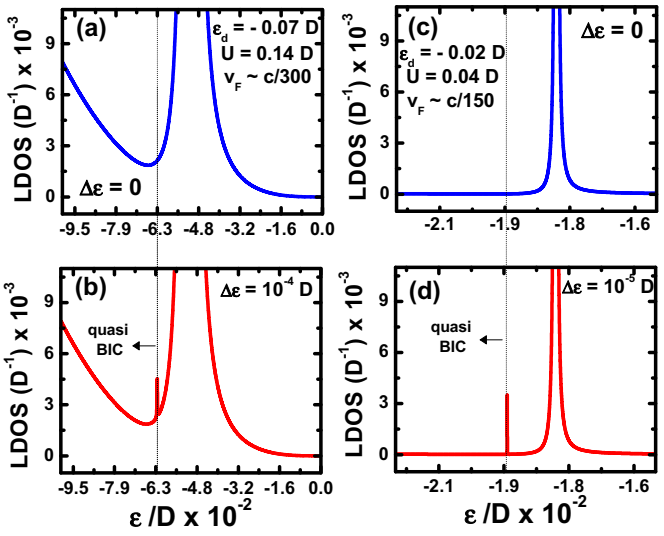

FIG. 3. (Color online) (a) $\mathcal{E}_d = -0.07D$, $\mathcal{U} = 0.14D, \mathcal{V} = 0.14D$, $v_F \approx c/300$, and $\triangle\mathcal{E} = 0$: LDOS in the region around the position of the BIC. The latter lies at $\mathcal{E} \approx -6.3 \times 10^{-2}D$ and is invisible in the LDOS; its position is shown by a vertical line. (b) The LDOS in the region around the position of the BIC for nonzero detuning between the energies of the upper and lower adatoms $\triangle\mathcal{E} = 10^{-4}D$; all other parameters are the same as in panel (a). One clearly sees that the BIC is reflected in the LDOS in the form of a tiny peak at $\mathcal{E} \approx -6.3 \times 10^{-2}D$ and thus should become detectable in transport measurements. (c) Same as panel (a), but for different values of the parameters: $\mathcal{E}_d = -0.02D$, $\mathcal{U} = 0.04D$, and $v_F \approx c/150$. (d) The LDOS in the region around the position of the BIC for nonzero detuning between the energies of the upper and lower adatoms $\triangle\mathcal{E} = 10^{-5}D$; all other parameters are the same as in panel (c).

In Fig. 3(a), we show the enlargement of the region wherein the peak around $\mathcal{E} \approx -6.3 \times 10^{-2}D$ is absent in the LDOS of Fig. 2(d), thus suggesting the existence of a BIC at this position. To make this BIC observable, one needs to introduce the coupling between it and the continuum states, which can be achieved by the introduction of a small detuning $\triangle\mathcal{E}$ between the energies of the upper and lower adatoms. As a matter of fact, this detuning will appear automatically due to the hybridizations of the STM tip with the adatoms, in particular when the former is found closer to the latter. In Fig. 3(b), we plot the LDOS for $\triangle\mathcal{E} = 10^{-4}D$. One clearly sees that a visible, although rather weak, peak appears at the energy corresponding to the BIC, in which a true BIC is transformed to a quasi-BIC detectable in transport experiments. Here we stress that within our theoretical framework, the role of the detuning $\triangle\mathcal{E}$ is the emulation of nonperturbative values for the

ratio t_{d1}/t_c, which forces the leaking of the BIC into the system energy continuum as the aftermath of the renormalization made by the STM tip on the level of the upper adatom. We should emphasize that Eq. (16), which describes this energy continuum as well as the conductance G through the system via Eq. (10), encloses fingerprints arising from Eq. (24) for the adatoms, such as the quasi-BIC near $\mathcal{E} \approx -6.3 \times 10^{-2} D$ that is observed in Fig. 3(b). This narrow state corresponds to that denoted by the resonance labeled (1) in Fig. 2(b), which leaks into the continuum of the system.

In the opposite situation, in which $\triangle\mathcal{E} = 0$, such a decay of the BIC is prevented due to the mechanism of Fano destructive interference pointed out previously. Thus Eq. (16) contains just the background contribution of Eq. (17) at $\mathcal{E} \approx -6.3 \times 10^{-2} D$, as Fig. 3(a) shows. In this case, the LDOS of the "graphene+adatoms" system behaves like that for the lattice of phantom atoms without adatoms. Thereby, if sharp resonances appear in both Eqs. (16) and (24) at the same position, they reveal the decay of the state within the adatoms into the energy continuum of the system: the sharp resonance appearing in the former equation is then considered a quasi-BIC. A quasi-BIC is characterized by a sharp resonance in Eq. (16) being detectable by the conductance G of Eq. (10), which indeed describes at $\mathcal{E} \approx -6.3 \times 10^{-2} D$ an electron that spends a long time in the vicinity of the adatom, whose wave function behaves like a Bloch state away from such a site.

Additionally, we clarify that a BIC is represented by the resonance belonging to the adatom under consideration since it appears via its DOS given by Eq. (24), but it is absent in Eq. (16), which determines the system conductance. It is worth noticing that despite the small but finite width $\Delta \propto |\mathcal{E}|^3$ of such a state in Eq. (24), which is visible around $\mathcal{E} \approx -6.3 \times 10^{-2} D$ in Fig. 2(b), the Fano destructive interference mechanism revealed in this work ensures that the state level is embedded in the continuum. This situation corresponds to electrons fully trapped within these adatoms in such a way that the decay rate $\sim \Delta/\hbar$ is suppressed.

On the other hand, the visibility of the quasi-BIC peak can be improved by approaching both levels $\mathcal{E}_d$ and $\mathcal{U}$ toward the Dirac points ($\mathcal{E}_d = -0.02D$ and $\mathcal{U} = 0.04D$) combined with the increasing of the Fermi velocity v_F ($v_F \approx c/150$) as shown in panels (c) and (d) of the same figure. From an experimental perspective, the tuning of the Fermi velocity can be performed by changing the dielectric constant in the substrate hosting the graphene sheet [28,29]. We should point out that the assumption of considering adatoms slightly off resonance, due to a detuning in energy levels for detection of quasi-BICs, was adopted in Ref. [23] for graphene ribbons. Here we apply the same procedure on our "graphene + adatoms" system in order to induce the decay of the BICs within the adatoms into the continuum of the aforementioned system.

In Fig. 4, we present the results for the case of the broken particle-hole symmetry, taking $\mathcal{U} = 0.035D$, $\mathcal{E}_d = -0.07D$, $v_F \approx c/300$, and $\triangle\mathcal{E} = 0$. By decreasing the Coulomb correlation energy from $\mathcal{U} = 0.14D$ to $0.035D$, it is possible to shift the peaks found within the conduction band ($\mathcal{E} > \mathcal{E}_F \equiv 0$) for the symmetric case $2\mathcal{E}_d + \mathcal{U} = 0$ into the valence band ($\mathcal{E} < \mathcal{E}_F \equiv 0$) as demonstrated in panel (a). Thus instead of the couple of peaks found in Fig. 2(b), four resonances appear within the valence band. Although the condition $2\mathcal{E}_d + \mathcal{U} = 0$ is no longer satisfied, the underlying physics remains: BICs emerge due to Fano antiresonances in the mixing term of the LDOS that suppress the corresponding peaks found in the diagonal term [see panels (a), (b), and (c), in which BICs are identified by vertical lines]. Panel (d) shows the band structure in such a case.

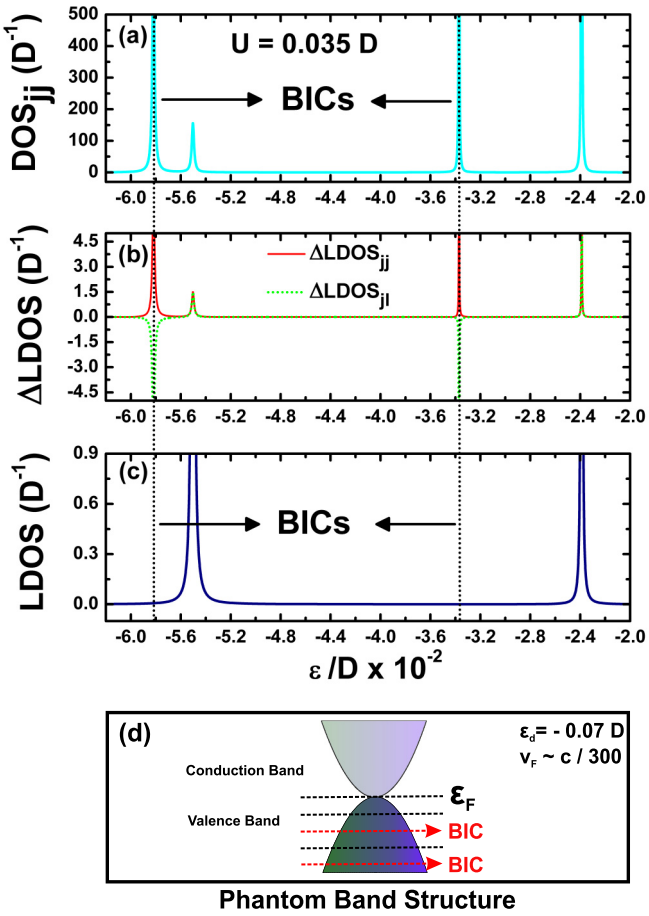

FIG. 4. (Color online) (a) Density of states for the pair of adatoms $\mathrm{DOS}_{jj} = \mathrm{DOS}_{11} = \mathrm{DOS}_{22}$ within the valence band. The parameters are $\mathcal{E}_d = -0.07D$, $\mathcal{U} = 0.035D$, $\mathcal{V} = 0.14D$, $v_F \approx c/300$, and $\triangle\mathcal{E} = 0$. Four peaks are present within the valence band, as $2\mathcal{E}_d + \mathcal{U} \neq 0$ particle-hole symmetry is broken. (b) Contributions to the LDOS of graphene from the adatom pair. The diagonal contribution shows four pronounced peaks, while the mixing term shows a couple of pronounced antiresonances. (c) Total LDOS revealing the BICs (marked by vertical lines) at positions where resonances of the diagonal term in the LDOS are compensated by the antiresonances in the mixing term. (d) Sketch of the energy diagram of the system.

Figure 5 depicts the analysis of the situation in which the adatoms are aligned with one of the carbon atoms of the lattice, as shown in panel (a). The parameters are the same as those employed in Fig. 2. One can find the expression for the LDOS using the field operator of a carbon atom [26],

$$\Psi_{\mathrm{carbon},\sigma} = \frac{1}{2\pi}\sqrt{\frac{\pi\Omega_0}{\mathcal{N}}}\sum_n \int \sqrt{|k|}\,dk\, c_{nk\sigma}\,, \qquad (34)$$

instead of the field operator of a phantom atom given by Eq. (9). The resulting LDOS is given by the same expressions

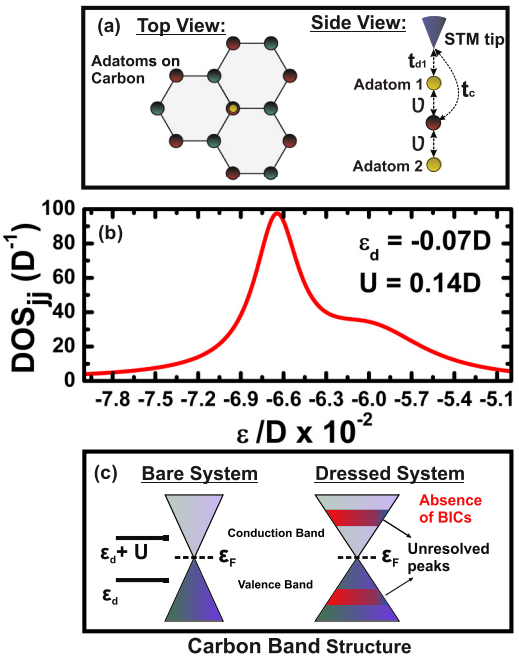

FIG. 5. (Color online) (a) Adatoms aligned with one of the carbon atoms. (b) $\mathcal{E}_d = -0.07D, \mathcal{U} = 0.14D, \mathcal{V} = 0.14D, v_F \approx c/300$, and $\triangle\mathcal{E} = 0$: $\mathrm{DOS}_{jj} = \mathrm{DOS}_{11} = \mathrm{DOS}_{22}$ of the adatoms in which unresolved peaks emerge, thus attesting that BICs cannot be formed in such a geometry. (c) Dirac cones persist exhibiting unresolved resonances simultaneously within the valence and conduction bands.

of Eqs. (16) and (18), with the only difference being that now $\mathcal{D}_0 \equiv \mathcal{D}_0^{\mathrm{carbon}} = \Omega_0|\mathcal{E}|/2\mathcal{N}\pi(\hbar v_F)^2$, $\Delta = \pi\mathcal{D}_0^{\mathrm{carbon}}\mathcal{V}^2$, and

$$\Sigma_{\mathrm{carbon}}(\mathbf{R}=\mathbf{0}) = \frac{\mathcal{V}^2}{D^2}\mathcal{E}\ln\left|\frac{\mathcal{E}^2}{D^2-\mathcal{E}^2}\right| - i\Delta \qquad (35)$$

stands for the self-energy [7] instead of that found in Eq. (23) for the phantom atom.

Figure 5(b) shows the DOS for the considered situation. One clearly sees that in contrast with the case of the phantom atom, BICs do not appear, since resolved peaks within $\mathrm{DOS}_{jj} = \mathrm{DOS}_{11} = \mathrm{DOS}_{22}$ are absent, and a couple of broad merged resonances appears instead. To explain such a behavior, let us focus on the Anderson broadening Δ. For the case of a phantom atom, $\Delta \propto |\mathcal{E}|^3$, and as the peaks at $\mathcal{E} \approx -6.3 \times 10^{-2} D$ and $\mathcal{E} \approx -5 \times 10^{-2} D$ denoted by (1) and (2) in Fig. 2(b) are found near the Dirac points ($\mathcal{E} = 0$), they are narrow enough in this region and can be easily resolved. For the case of the collinear alinement of the impurities with one of the carbon atoms, $\Delta \propto |\mathcal{E}|$, thereby the broadening of the peaks in the vicinity of the Dirac points increases and they become unresolved, as seen in Fig. 5(b). Figure 5(c) displays a sketch of the Dirac cones in such a situation.

IV. CONCLUSIONS

In summary, we have demonstrated that BICs can appear in a system consisting of a graphene sheet and a collinear pair of adatoms placed above and below the center of the hexagonal cell, where a fictitious or phantom atom emulates the six carbon atoms of the cell. The effect is due to the destructive Fano interference assisted by Coulomb correlations in the adatoms. We have checked that BICs do not appear if Coulomb interaction is absent or if adatoms are collinear with one of the carbon atoms in the lattice.

ACKNOWLEDGMENTS

This work was supported by the agencies CNPq, CAPES, 2014/14143-0 São Paulo Research Foundation (FAPESP), FP7 IRSES project QOCaN, and the Rannis project "Bose and Fermi systems for spintronics." A.C.S. thanks the Nanyang Technological University at Singapore for hospitality.

[1] K. S. Novoselov, Rev. Mod. Phys. **83**, 837 (2011).
[2] N. M. R. Peres, Rev. Mod. Phys. **82**, 2673 (2010).
[3] A. H. Castro Neto, F. Guinea, N. M. R. Peres, K. S. Novoselov, and A. K. Geim, Rev. Mod. Phys. **81**, 109 (2009).
[4] T. Eelbo, M. Wasniowska, M. Gyamfi, S. Forti, U. Starke, and R. Wiesendanger, Phys. Rev. B **87**, 205443 (2013).
[5] T. Eelbo, M. Wasniowska, P. Thakur, M. Gyamfi, B. Sachs, T. O. Wehling, S. Forti, U. Starke, C. Tieg, A. I. Lichtenstein, and R. Wiesendanger, Phys. Rev. Lett. **110**, 136804 (2013).
[6] X. Liu, C. Z. Wang, Y. X. Yao, W. C. Lu, M. Hupalo, M. C. Tringides, and K. M. Ho, Phys. Rev. B **83**, 235411 (2011).
[7] B. Uchoa, V. N. Kotov, N. M. R. Peres, and A. H. Castro Neto, Phys. Rev. Lett. **101**, 026805 (2008).
[8] B. Uchoa, L. Yang, S.-W. Tsai, N. M. R. Peres, and A. H. Castro Neto, Phys. Rev. Lett. **103**, 206804 (2009).
[9] B. Uchoa, L. Yang, S.-W. Tsai, N. M. R. Peres, and A. H. Castro Neto, New J. Phys. **16**, 013045 (2014).
[10] P. D. Gorman, J. M. Duffy, M. S. Ferreira, and S. R. Power, Phys. Rev. B **88**, 085405 (2013).
[11] E. Kogan, Phys. Rev. B **84**, 115119 (2011).
[12] M. Ternes, A. J. Heinrich, and W.-D. Schneider, J. Phys.: Condens. Matter **21**, 053001 (2009).
[13] A. E. Miroshnichenko, S. Flach, and Y. S. Kivshar, Rev. Mod. Phys. **82**, 2257 (2010).
[14] J. von Neumann and E. Wigner, Phys. Z. **30**, 465 (1929).
[15] F. H. Stillinger and D. R. Herrick, Phys. Rev. A **11**, 446 (1975).
[16] C. W. Hsu, B. Zhen, J. Lee, S.-L. Chua, S. G. Johnson, J. D. Joannopoulos, and M. Soljačić, Nature (London) **499**, 188 (2013).
[17] Y. Boretz, G. Ordonez, S. Tanaka, and T. Petrosky, Phys. Rev. A **90**, 023853 (2014).
[18] Y. Plotnik, O. Peleg, F. Dreisow, M. Heinrich, S. Nolte, A. Szameit, and M. Segev, Phys. Rev. Lett. **107**, 183901 (2011).
[19] A. Crespi, L. Sansoni, G. Della Valle, A. Ciamei, R. Ramponi, F. Sciarrino, P. Mataloni, S. Longhi, and R. Osellame, Phys. Rev. Lett. **114**, 090201 (2015).
[20] J. Mur-Petit and R. A. Molina, Phys. Rev. B **90**, 035434 (2014).
[21] G. Della Valle and S. Longhi, Phys. Rev. B **89**, 115118 (2014).

[22] C. González-Santander, P. A. Orellana, and F. Domínguez-Adame, Europhys. Lett. **102**, 17012 (2013).
[23] J. W. González, M. Pacheco, L. Rosales, and P. A. Orellana, Europhys. Lett. **91**, 66001 (2010).
[24] W.-J. Gong, X.-Y. Sui, Y. Wang, G.-D. Yu, and X.-H. Chen, Nanoscale Res. Lett. **8**, 330 (2013).
[25] J. Hubbard, Proc. R. Soc. London, Ser. A **281**, 401 (1964).
[26] Z.-G. Zhu, K.-H. Ding, and J. Berakdar, Europhys. Lett. **90**, 67001 (2010).
[27] L. Li, Y.-Y. Ni, Y. Zhong, T.-F. Fang, and H.-G. Luo, New J. Phys. **15**, 053018 (2013).
[28] C. Hwang, D. A. Siegel, S.-K. Mo, W. Regan, A. Ismach, Y. Zhang, A. Zettl, and A. Lanzara, Sci. Rep. **2**, 590 (2012).
[29] D. A. Siegel, W. Regan, A. V. Fedorov, A. Zettl, and A. Lanzara, Phys. Rev. Lett. **110**, 146802 (2013).